ACS APPLIED MATERIALS & INTERFACES

Research Article

www.acsami.org

Self-Assembly of Crystalline Structures of Magnetic Core–Shell Nanoparticles for Fabrication of Nanostructured Materials

Xiaozheng Xue,[†] Jianchao Wang,[†] and Edward P. Furlani*[,†,‡]

[†]Department of Chemical and Biological Engineering and [‡]Department of Electrical Engineering, University at Buffalo SUNY, Buffalo, New York 14260, United States

ABSTRACT: A theoretical study is presented of the template-assisted formation of crystalline superstructures of magnetic–dielectric core–shell particles. The templates produce highly localized gradient fields and a corresponding magnetic force that guides the assembly with nanoscale precision in particle placement. The process is studied using two distinct and complementary computational models that predict the dynamics and energy of the particles, respectively. Both mono- and polydisperse colloids are studied, and the analysis demonstrates for the first time that although the particles self-assemble into ordered crystalline superstructures, the particle formation is not unique. There is a Brownian motion-induced degeneracy in the process wherein various distinct, energetically comparable crystalline structures can form for a given template geometry. The models predict the formation of hexagonal close packed (HCP) and face centered cubic (FCC) structures as well as mixed phase structures due to in-plane stacking disorders, which is consistent with experimental observations. The polydisperse particle structures are less uniform than the monodisperse particle structures because of the irregular packing of different-sized particles. A comparison of self-assembly using soft- and hard-magnetic templates is also presented, the former being magnetized in a uniform field. This analysis shows that soft-magnetic templates enable an order-of-magnitude more rapid assembly and much higher spatial resolution in particle placement than their hard-magnetic counterparts. The self-assembly method discussed is versatile and broadly applies to arbitrary template geometries and multilayered and multifunctional mono- and polydisperse core–shell particles that have at least one magnetic component. As such, the method holds potential for the bottom-up fabrication of functional nanostructured materials for a broad range of applications. This work provides unprecedented insight into the assembly process, especially with respect to the viability and potential fundamental limitations of realizing structure-dependent material properties for applications.

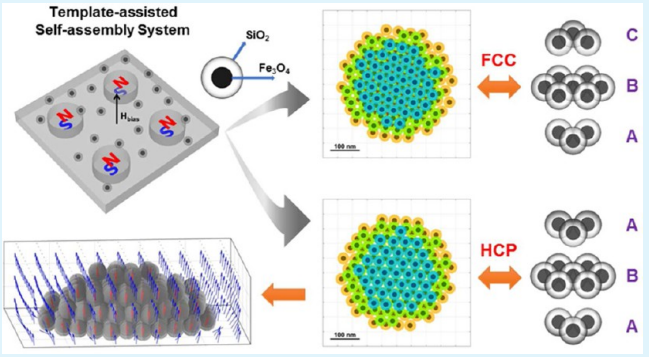

KEYWORDS: *field-directed assembly, magnetic template-assisted self-assembly, assembly of core–shell particles, assembly of crystalline superstructures, magnetic dipole–dipole interactions*

INTRODUCTION

Advances in nanotechnology, especially in the synthesis of multifunctional nanoparticles, have opened up opportunities for the bottom-up fabrication of nanostructured materials with extraordinary properties. Bottom-up nanofabrication has potential advantages over top-down lithographic-based methods in terms of scalability, throughput and cost. Self-assembly is among the most promising methods for bottom-up nanofabrication[1,2] and has been used for the development of magnetic,[3] photonic,[4] micro-optical,[5] and electronic[6] materials. Directed and template-assisted self-assembly methods are especially enabling as they provide enhanced control over particle placement and the formation of extended particle structures.[7−11] The use of such methods for magnetic nanoparticles is of particular interest as ordered structures of such particles hold potential for transformative advances in a broad range of technologies including data storage, telecommunications, sensors, actuators, biomedicine, MEMS, etc. To date, various groups have demonstrated the self-assembly of magnetic nanoparticles with nanoscale[10,11] and microscale[8,12,13] resolution using uniform and/or gradient fields as well as the field-induced self-assembly of magnetic core–shell particles.[14] Of particular relevance to this work is that of Henderson et al.,[10] which demonstrates template-assisted self-assembly of magnetic nanoparticles using a combination of a spatially alternating gradient field (provided by a patterned magnetized template within a magnetic recording medium) and a uniform bias field. The self-assembled particle patterns were transferred from the substrate to a polymer film and lifted off for use as a stand-alone functional material, for example, diffraction grating.[15] A similar approach has recently been demonstrated by Mohtasebzadeh Abdul et al.[16] Although interest in self-assembly-based nanofabrication is growing rapidly, many of the fundamental mechanisms of the underlying processes are

Received: July 24, 2015
Accepted: September 21, 2015
Published: September 21, 2015

DOI: 10.1021/acsami.5b08310
ACS Appl. Mater. Interfaces 2015, 7, 22515−22524

poorly understood and rational design is lacking. In this regard, the self-assembly of 3D ordered (crystalline) particle structures with nanoscale resolution remains particularly challenging.

In this paper we present a theoretical study of the template-assisted self-assembly of crystalline superstructures of magnetic−dielectric core−shell nanoparticles. In our previous work we demonstrated that such structures can form in milliseconds with nanoscale resolution using soft-magnetic, for example, lithographically formed, template elements in the presence of a uniform bias field as shown in Figure 1.[17,18] However, the uniqueness of the assembled structure was heretofore not considered. In this paper we perform a theoretical study to resolve this issue using two distinct and complementary computational models. The models are based on Langevin's equation and the Monte Carlo method and predict the dynamics and energy of the particles, respectively. Although these models are well suited for our study, it should be noted that a variety of other modeling approaches are commonly used to predict the field-directed transport and self-assembly of magnetic particles. These include Brownian dynamics,[19,20] the discrete element method,[21] the lattice−Boltzmann method,[22] Monte Carlo[23,24] analysis, molecular dynamic simulations,[25] stochastic dynamics,[26] and various analytical methods.[27−29]

We use Langevin and Monte Carlo models to study both mono- and ploydisperse colloids, and the analysis demonstrates for the first time that there is a Brownian motion-induced degeneracy in the assembly process, wherein the assembled particles can take the form of distinct, energetically comparable crystalline superstructures. Specifically, for a given template geometry, the models predict the formation of hexagonal closed packed (HCP) and face centered cubic (FCC) structures as well as mixed phase HCP/FCC structures that form due to in-plane stacking disorders. Although these various crystalline structures had been observed experimentally, the underlying causal mechanisms, which we quantify for the first time in this work, were not well understood. We also compare the self-assembly of monodisperse particles using soft- and hard-magnetic templates. We demonstrate for the first time that soft-magnetic templates, combined with a uniform magnetizing field, enable an order-of-magnitude faster (~20 ms) assembly with much higher spatial resolution than their hard-magnetic counterparts. This is due to the combined effects of the uniform bias field and the localized gradient fields produced by the templates. Specifically, the bias field induces saturated dipole moments in the particles and a uniform orientation, whereas the combination of uniform and gradient fields produces highly localized regions of attractive and repulsive force that enable superior control of particle placement during assembly.[17,18] The hard-magnetic templates produce a comparably weaker and purely attractive magnetic force field distribution that results in slower assembly and less precision in particle placement. Finally, the self-assembly method that we study is very versatile and broadly applies to arbitrary template geometries and multilayered mono- and polydisperse core−shell particles that have at least one magnetic component. It holds potential for the cost-effective fabrication of functional nanostructured materials for many diverse technological applications. This work provides unprecedented insight into the assembly process, especially with respect to potential fundamental limitations in realizing crystalline structure-dependent material properties for such applications.

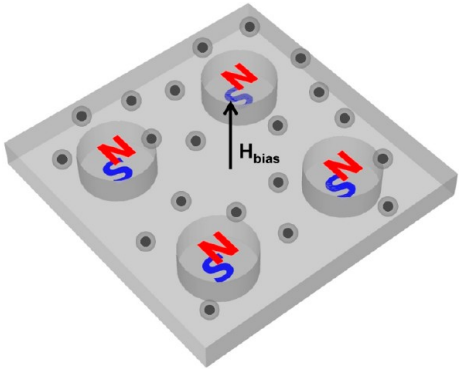

Figure 1. Template-assisted self-assembly system showing colloidal core−shell nanoparticles above a substrate that contains a 2D array of embedded soft-magnetic cylindrical template elements.

COMPUTATIONAL MODELS

Langevin Model. We use Langevin's equation to predict particle motion during assembly

$$m_i\frac{d^2x_i}{dt^2} = \boldsymbol{F}_{mag,i} + \boldsymbol{F}_{vis,i} + \boldsymbol{F}_{B,i}(t) + \sum_{\substack{j=1 \\ j\neq i}}^{N} (\boldsymbol{F}_{dd,ij} + \boldsymbol{F}_{vdw,ij} + \boldsymbol{F}_{surf,ij} + \boldsymbol{F}_{hyd,ij}) \quad (1)$$

where m_i and $x_i(t)$ are the mass and position of the ith particle. The right-hand side of eq 1 represents the sum of forces on a particle including magnetic, hydrodynamic, and dipole−dipole forces, Brownian diffusion, van der Waals force, and effects of surfactants. The details of this model and its application can be found in our previous work.[17,18] Briefly, the interparticle forces give rise to a coupled system of ODEs, one equation for each colloidal particle. We reduce the system of second-order equations (eq 1) to a system of coupled first-order equations for the velocity and displacement of the particles. We solve these using a dynamic time-stepping approach that greatly accelerates and stabilizes the solution. The discretized coupled equations are of the form

$$\boldsymbol{v}_{i,f} = \frac{\boldsymbol{F}_{sum,i}}{D_i} + \left(\boldsymbol{v}_{i,0} - \frac{\boldsymbol{F}_{sum,i}}{D_i}\right) e^{-D_i/m_i\tau} \quad (2)$$

$$\Delta\boldsymbol{x}_i = \frac{\boldsymbol{F}_{sum,i}}{D_i}\tau + \frac{m_i}{D_i}\left(\boldsymbol{v}_{i,0} - \frac{\boldsymbol{F}_{sum,i}}{D_i}\right)(1 - e^{-D_i/m_i\tau}) \quad (3)$$

where $D_i = 6\pi\eta R_{hyd,p,i}$ is the drag coefficient (η is the fluid viscosity and $R_{hyd,p,i}$ is the hydrodynamic radius of the ith particle), τ is the integration time step, and $\boldsymbol{v}_{i,0}$ and $\boldsymbol{v}_{i,f}$ are the velocity of the ith particle at the beginning and end of the time step and

$$\boldsymbol{F}_{sum,i} = \boldsymbol{F}_{mag,i} + \boldsymbol{F}_{B,i}(t) + \sum_{\substack{j=1 \\ j\neq i}}^{N} (\boldsymbol{F}_{dd,ij} + \boldsymbol{F}_{vdw,ij} + \boldsymbol{F}_{surf,ij} + \boldsymbol{F}_{hyd,ij}) \quad (4)$$

In our analysis τ is dynamically adjusted on the basis of the relative velocities and surface-to-surface separations h_{ij} of the particles. The various force terms in the model are described in detail in our previous work and are briefly summarized for convenience.

DOI: 10.1021/acsami.5b08310
ACS Appl. Mater. Interfaces 2015, 7, 22515−22524

Magnetic Force. The magnetic force is predicted using an "effective" dipole moment method in which the particle is modeled as an "equivalent" point dipole with an effective moment $\boldsymbol{m}_{\mathrm{eff},i}$. The force on the ith particle is given by[27]

$$\boldsymbol{F}_{\mathrm{mag},i} = \mu_{\mathrm{f}}(\boldsymbol{m}_{i,\mathrm{eff}}\cdot\nabla)\boldsymbol{H}_{\mathrm{a}} \tag{5}$$

where μ_{f} is the permeability of the fluid. H_{a} is the applied magnetic field intensity at the center of the particle. Here, H_{a} is a superposition of a uniform bias field and template-induced gradient fields, that is, $\boldsymbol{H}_{\mathrm{a}} = \boldsymbol{H}_{\mathrm{bias}} + \boldsymbol{H}_{\mathrm{template}}$. The moment is given by $\boldsymbol{m}_{\mathrm{eff},i} = V_{p,i}\,M_p$, where $V_{p,i}$ and M_p are the volume and magnetization of particle i, respectfully. For magnetic−dielectric core−shell particles, only the core contributes to that magnetic force and, consequently, $\boldsymbol{m}_{\mathrm{eff},i} = V_{\mathrm{core},i}\,M_p$. The moment can be determined using a magnetization model that takes into account self-demagnetization and magnetic saturation of the particles[27,28]

$$\boldsymbol{m}_{i,\mathrm{eff}} = V_{\mathrm{core},i} f(H_{\mathrm{a}})\boldsymbol{H}_{\mathrm{a}} \tag{6}$$

where[30]

$$f(H_{\mathrm{a}}) = \begin{cases} \dfrac{3(\chi_{\mathrm{p}} - \chi_{\mathrm{f}})}{(\chi_{\mathrm{p}} + 2\chi_{\mathrm{f}}) + 3} & H_{\mathrm{a}} < \left(\dfrac{(\chi_{\mathrm{p}} + 2\chi_{\mathrm{f}}) + 3}{3(\chi_{\mathrm{p}} - \chi_{\mathrm{f}})}\right)M_{\mathrm{sp}} \\ M_{\mathrm{sp}}/H_{\mathrm{a}} & H_{\mathrm{a}} \geq \left(\dfrac{(\chi_{\mathrm{p}} + 2\chi_{\mathrm{f}}) + 3}{3(\chi_{\mathrm{p}} - \chi_{\mathrm{f}})}\right)M_{\mathrm{sp}} \end{cases} \tag{7}$$

In this expression, χ_{f} is the susceptibility of the fluid and χ_{p} is the intrinsic magnetic susceptibility of the particle, i.e. $M_{\mathrm{p}} = \chi_{\mathrm{p}}H_{\mathrm{in}}$ where H_{in} is the field inside the particle. H_{in} differs from H_{a} by the demagnetization field. that is, $H_{\mathrm{in}} = H_{\mathrm{a}} - N_{\mathrm{d}}M_{\mathrm{p}}$, where N_{d} is the demagnetization factor of the particle, that is, $N_{\mathrm{d}} = 1/3$ for a spherical particle. The value of χ_{p} can be obtained from a measured M versus H curve. However, M is often plotted as a function of H_{a}, in which case $M_{\mathrm{p}} = \chi_{\mathrm{a}}H_{\mathrm{a}}$, where χ_{a} is the apparent susceptibility. The two values of susceptibility are related as follows: $\chi_{\mathrm{p}} = \chi_{\mathrm{a}}/(1 - N_{\mathrm{d}}\chi_{\mathrm{a}})$, which reduces to $\chi_{\mathrm{p}} = 3\chi_{\mathrm{a}}/(3 - \chi_{\mathrm{a}})$ for a spherical particle.[31] Thus, the magnetic force can be rewritten as

$$\boldsymbol{F}_{\mathrm{mag},i} = \mu_{\mathrm{f}}V_{\mathrm{core},i}f(H_{\mathrm{a}})(\boldsymbol{H}_{\mathrm{a}}\cdot\nabla)\boldsymbol{H}_{\mathrm{a}} \tag{8}$$

Magnetic Dipole−Dipole Interaction. The dipole−dipole force in eq 1 is obtained from the gradient of a potential $U_{\mathrm{dd},ij}$

$$\boldsymbol{F}_{\mathrm{dd},ij} = -\nabla U_{\mathrm{dd},ij} \tag{9}$$

where

$$U_{\mathrm{dd},ij} = -\frac{\mu_{\mathrm{f}}}{4\pi}\left(3\frac{(\boldsymbol{m}_{i,\mathrm{eff}}\cdot\boldsymbol{r}_{ij})(\boldsymbol{m}_{j,\mathrm{eff}}\cdot\boldsymbol{r}_{ij})}{r_{ij}^5} - \frac{\boldsymbol{m}_{i,\mathrm{eff}}\cdot\boldsymbol{m}_{j,\mathrm{eff}}}{r_{ij}^3}\right) \tag{10}$$

and $\boldsymbol{m}_{i,\mathrm{eff}}$ and $\boldsymbol{m}_{j,\mathrm{eff}}$ are the moments of the ith and jth particles, respectively, and $\boldsymbol{r}_{ij}$ is the displacement vector between them. Note that $\boldsymbol{F}_{\mathrm{dd},ij} \propto R_{\mathrm{core}}^6$ for identical core−shell particles.

Van der Waals Interaction. Van der Waals force is taken into account as an attractive force, which is calculated using[32]

$$\boldsymbol{F}_{\mathrm{vdw},ij} = \frac{32}{3}\frac{A\cdot(R_{p,i}\cdot R_{p,j})^3\cdot r_{ij}}{(r_{ij}^2 - (R_{p,i} + R_{p,j})^2)^2(r_{ij}^2 - (R_{p,i} - R_{p,j})^2)^2} \tag{11}$$

where A is the Hamaker constant and $R_{p,i}$ and $R_{p,j}$ are the radii of the ith and jth particles, respectively.

Surfactant Force. The repulsive force between two particles due to surfactant−surfactant contact is derived from a potential U_{s}

$$\boldsymbol{F}_{\mathrm{surf},ij} = -\nabla U_{\mathrm{s}} \tag{12}$$

where[33]

$$U_{\mathrm{s}} = 2\pi\frac{R_{p,i}^2\cdot R_{p,j}^2}{(R_{p,i} + R_{p,j})^2}N_{\mathrm{s}}k_{\mathrm{B}}T\left\{2 - \frac{r_{ij} - (R_{p,i} + R_{p,j})}{\bar{\delta}} - \frac{r_{ij}}{\bar{\delta}}\ln\left(\frac{(R_{p,i} + R_{p,j}) + 2\bar{\delta}}{r_{ij}}\right)\right\} \tag{13}$$

and $\bar{\delta}$ and N_{s} are the average thickness of the surfactant layer and the surface density of surfactant molecules, respectively.

Viscous Drag. The drag force on a particle is computed using Stokes' formula

$$\boldsymbol{F}_{\mathrm{vis},i} = D_i\frac{\mathrm{d}\boldsymbol{x}_i}{\mathrm{d}t} \tag{14}$$

where $D_i = 6\pi\eta R_{\mathrm{hyd},p,i}$ is described above in eq 2.

Interparticle Hydrodynamics Interactions. Hydrodynamic interactions between particles become important at small surface-to-surface separation distances. The force between two neighboring particles is based on lubrication theory and given by[32]

$$\boldsymbol{F}_{\mathrm{hyd},ij} = \frac{6\pi\mu_{\mathrm{f}}V_{\mathrm{r},i,j}}{h_{ij}}\frac{R_{p,i}^2\cdot R_{p,j}^2}{(R_{p,i} + R_{p,j})^2} \tag{15}$$

where h_{ij} is the separation between the surfaces and $\boldsymbol{V}_{\mathrm{r},ij}$ is the relative velocity between the particles. When the particles are in contact ($h_{ij} \leq 0$), this force is considered to be negligible.

Brownian Motion. The Brownian force in one dimension was modeled as a Gaussian white noise process

$$F_{\mathrm{B,i}} = \xi\sqrt{\frac{2D_ik_{\mathrm{B}}T}{\Delta t}} \tag{16}$$

where k_{B} is Boltzmann's constant, D_i is the Stokes' drag coefficient as described above, and ξ is a random number with a Gaussian distribution. The 3D Brownian force is obtained by applying eq 16 for each force component.

Monte Carlo Model. Simulations were performed using the Monte Carlo method with the Metropolis algorithm to determine the final equilibrium particle structures. The approach was as follows. First, an initial configuration is generated consisting of randomly distributed particles. Each particle is then subjected to a random walk with a limited displacement step to generate a new position (x_{new}, y_{new}, z_{new}) in the particle trail. The change in the total energy ΔU between new and initial configurations is then evaluated on the basis of the particle displacement. The total energy U includes the magnetostatic and magnetic dipole−dipole energies, van der Waals potential energy, and a surfactant energy that is computed when the particles are in contact. A uniform random number δ is generated with $0 < \delta < 1$, and if $\delta < \exp(-\Delta U/k_{\mathrm{B}}T)$, the particle displacement is accepted and the new particle configuration is adopted. This process is repeated until equilibrium is reached.

DOI: 10.1021/acsami.5b08310
ACS Appl. Mater. Interfaces 2015, 7, 22515−22524

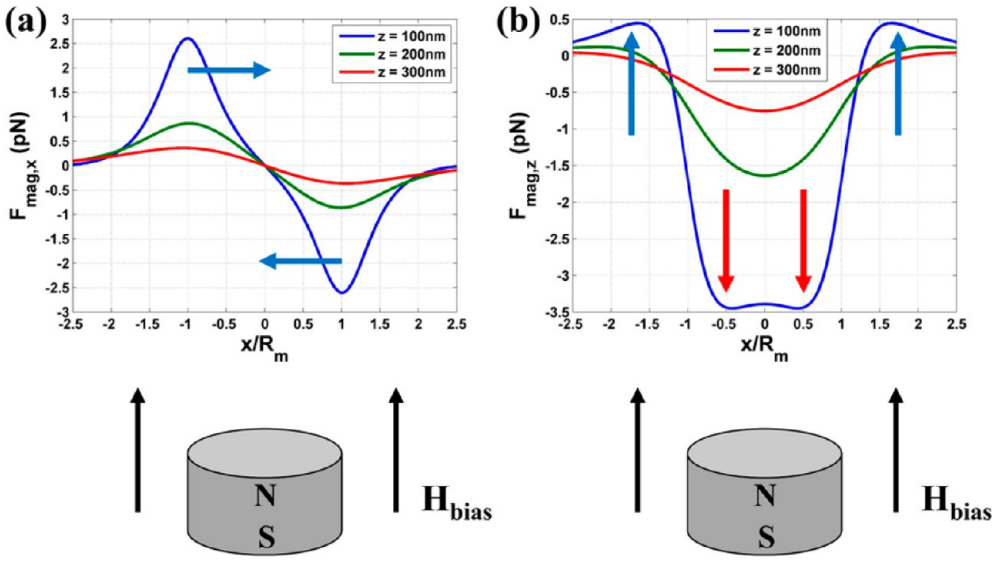

Figure 2. Magnetic force along horizontal lines 100, 200, and 300 nm above a soft-magnetic template (arrows indicate direction of force): (a) $F_{mag,x}$; (b) $F_{mag,z}$.

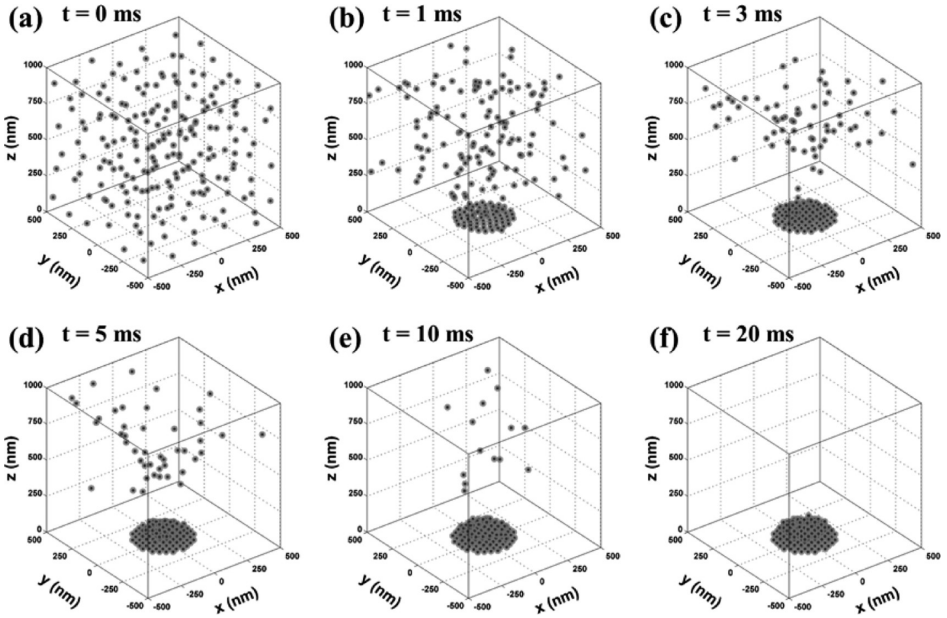

Figure 3. Self-assembly dynamics for HCP as presented in images showing particles at various times during the assembly: (a) t = 0 ms; (b) t = 1 ms; (c) t = 3 ms; (d) t = 5 ms; (e) t = 10 ms; (f) t = 20 ms.

Analysis of Self-Assembly. We first use the Langevin and Monte Carlo models to study the self-assembly of monodisperse magnetic−dielectric core−shell nanoparticles. For the purpose of analysis, we consider Fe_3O_4−SiO_2 particles with a core diameter of 17 nm and a total particle diameter of 40 nm, similar to those synthesized by Ding.[34] The magnetic templates consist of a 2D array of nanocylinders embedded in a nonmagnetic substrate as shown in Figure 1. The soft-magnetic templates are assumed to be permalloy (78% Ni, 22% Fe) with a saturation magnetization $M_{e,s} = 8.6 \times 10^5$ A/m. The radius and height of the cylinders are R_m = 200 nm and h = 300 nm, respectively, and they are spaced 1 μm apart center-to-center so that there is negligible overlap in their respective fields.[17,18] A uniform bias field of $H_{bias} = 3.9 \times 10^5$ A/m is applied to saturate the cylinders. It should be noted that field will also saturate the magnetic core of the particles. The hard-magnetic elements have the same size, position, and level of magnetization as the permalloy elements, but no bias field is required as they are permanently magnetized. The carrier fluid has the same properties as water.

The particle assembly is driven by the magnetic force, and it is instructive to examine this in some detail to gain insight into the process. It suffices to consider a single element as there is negligible overlap of the template fields given their separation.[17,18] We first consider a soft-magnetic element in a uniform bias field and compute the x and z force components along a horizontal line, that is, -500 nm $\leq x \leq$ 500 nm, that spans its diameter. The field components are evaluated at three different heights, z = 100, 200, and 300 nm, above the element as shown in Figure 2. From Figure 2a we find that the radial force $F_{mag,x}$ is directed inward toward the center of the cylinder as indicated by the blue arrows. This acts to focus the particles over the

DOI: 10.1021/acsami.5b08310
ACS Appl. Mater. Interfaces 2015, 7, 22515−22524

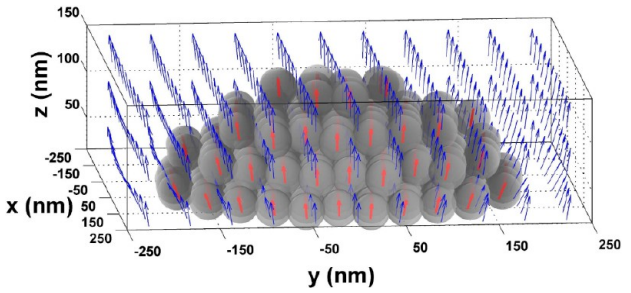

Figure 4. Particle packing and orientation of magnetic moments (red) and external field distribution (blue) for a HCP structure.

cylinder during assembly and produces a tapered particle structure as reported in the literature.[9] The axial force $F_{mag,z}$, shown in Figure 2b, is relatively strong and attractive (red arrows) over the center of the element, $x/R_m \leq 1$, which promotes assembly in this region. However, there is also a relatively weak repulsive axial force (blue arrows) near the edge of the cylinder ($r = R_m$) that prevents particles from assembling just outside the outer edge of the cylinder. The localized regions of attractive and repulsive force are a key feature of soft-magnetic template-driven assembly that enables nanoscale precision of particle placement as described in our previous work.[17,18]

We use Langevin's equation (eq 1) to study the dynamics of the colloidal Fe_3O_4−SiO_2 particles dispersed in a 1 μm^3 unit cell (with periodic boundary conditions), under the influence of the force provided by the soft-magnetic element system. The particles are initially randomly distributed and occupy a volume fraction of 0.67%. Upon running several simulations, we found that although the particles assemble into an ordered crystalline superstructure, the final particle configuration is not unique. Specifically, the particles randomly assemble into HCP and FCC structures as well as mixed HCP/FCC structures due to an in-plane stacking disorder,[35] which is consistent with experimental observations.[9] Simulation images for the HCP structure showing the positions of the particles at various stages of assembly are shown in Figure 3. The final assembly is completed in 20 ms and has a tapered profile with a partially populated fourth layer as shown in Figures 4 and 5. The packing of the particles is shown in Figure 4, along with the orientations of their magnetic moments. A more detailed image showing a color-coded particle packing of the various HCP layers is shown in Figure 5. Corresponding figures for a simulation that resulted in an FCC structure are shown in Figure 6.

A mixed phase structure is shown in Figure 7. This has an in-plane stacking disorder[35] (linear defect) in the second layer that is evident in Figure 7b. This defect leads to a third layer that contains mixed HCP (lower right corner) and FCC (upper left corner) particle configurations above the defect as shown in Figure 7c.

As a means of validating these predictions, we simulated the same process using the Monte Carlo method as described above. This analysis confirmed the random formation of HCP and FCC structures, and representative particle configurations are shown in Figure 8. To understand the degeneracy of the assembled structure, we computed the average energy per particle E_p in the final equilibrium configuration and expressed this as a multiple of the thermal energy per particle. For the HCP and FCC structures we have $E_{p,HCP} = -243.15 \times k_B T$ and

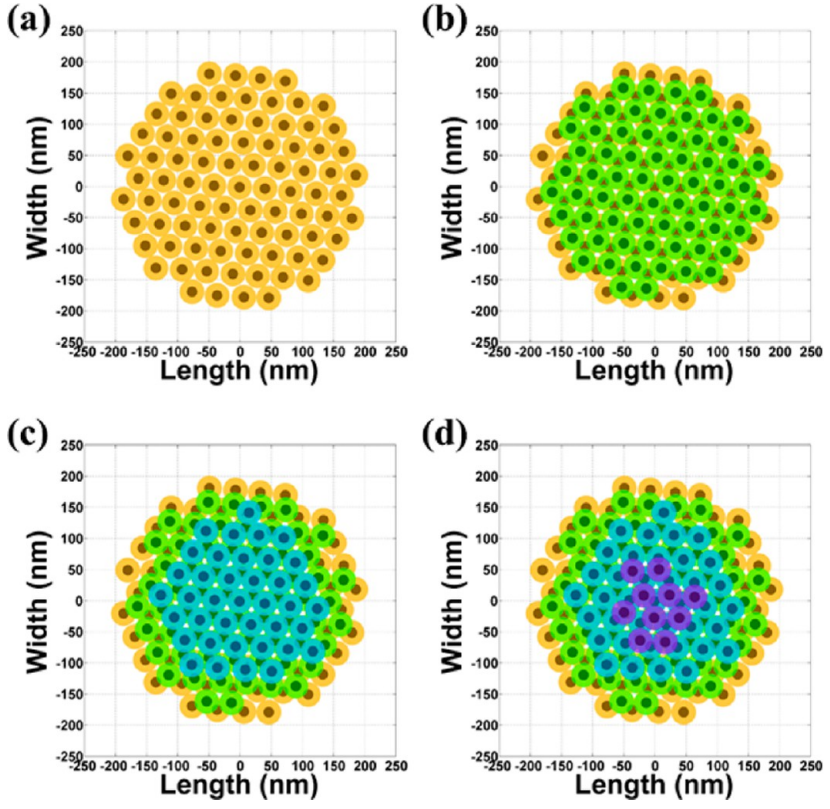

Figure 5. Multilayer HCP structure: (a, b, c, and d) first, second, third, and fourth layers of the assembled structure; the core is a solid sphere, and the shell is semitransparent.

DOI: 10.1021/acsami.5b08310
ACS Appl. Mater. Interfaces 2015, 7, 22515−22524

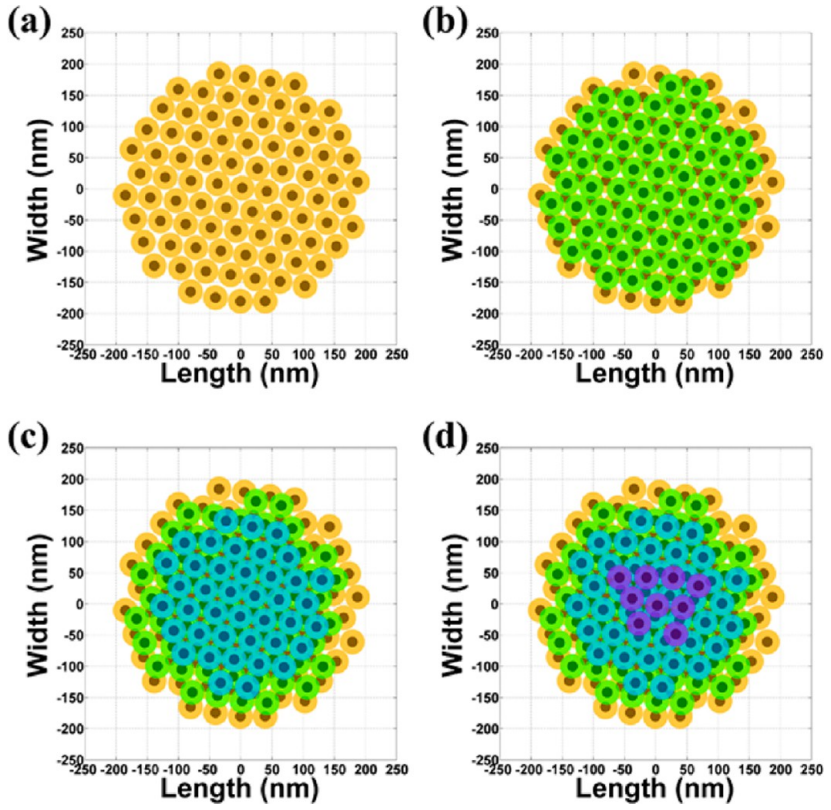

Figure 6. Multilayer FCC structure: (a, b, c, and d) first, second, third, and fourth layers of the assembled structure; the core is a solid sphere, and the shell is semitransparent.

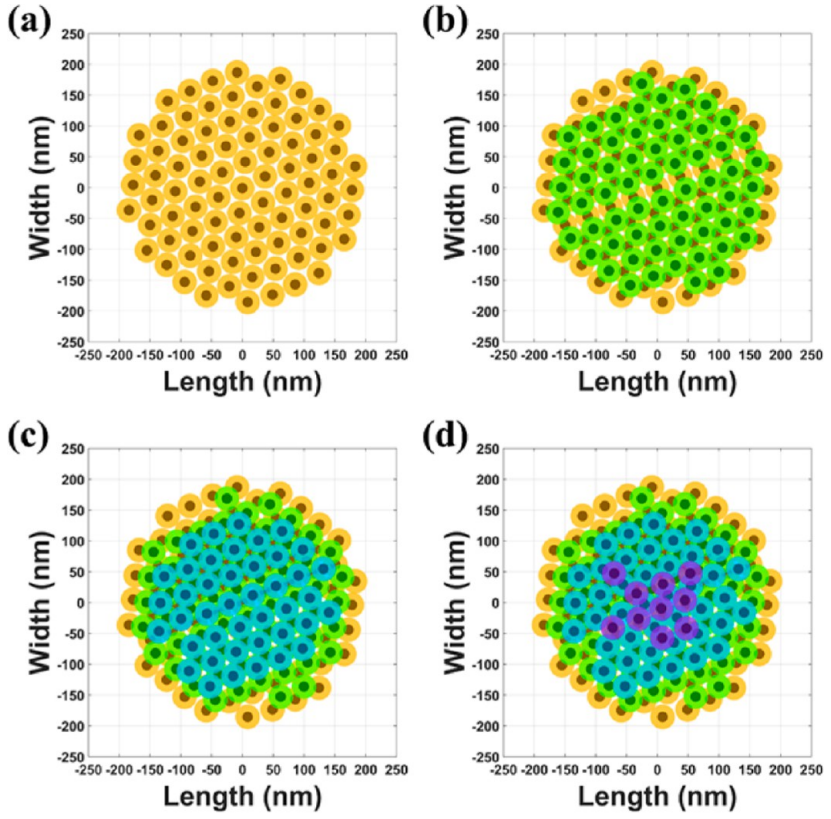

Figure 7. Multilayer mixed phase structure: (a, b, c, and d) first, second, third, and fourth layers of the assembled structure; the core is a solid sphere, and the shell is semitransparent.

DOI: 10.1021/acsami.5b08310
ACS Appl. Mater. Interfaces 2015, 7, 22515−22524

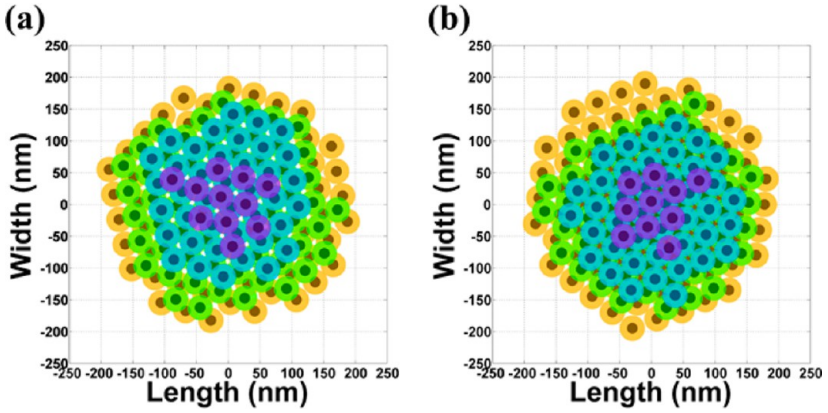

Figure 8. Monte Carlo simulation: (a) HCP; (b) FCC structures.

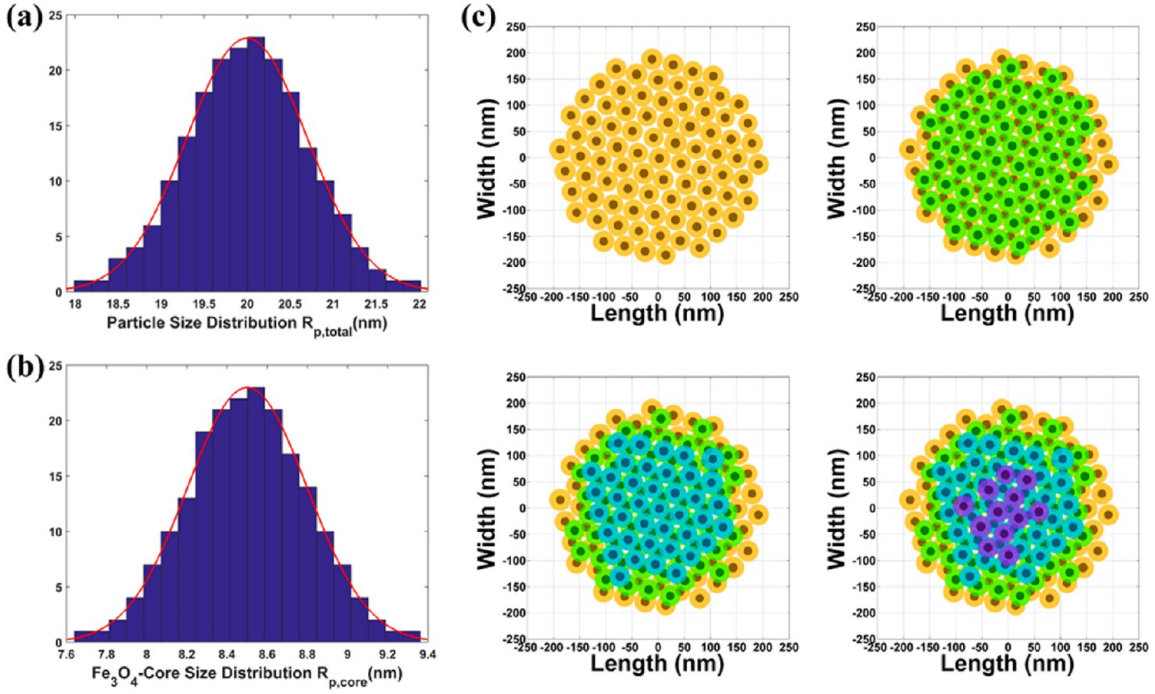

Figure 9. Multilayer HCP structure with 10% size-dispersed particles: (a) whole particle size distribution; (b) Fe_3O_4-core size distribution; (c) multilayer HCP structure, first, second, third, and fourth layers of the assembled structure, respectively.

$E_{p,FCC} = -243.45 \times k_BT$. The energy difference per particle between these two configurations is only 20% of a particle's thermal energy. Thus, there is a Brownian motion-induced degeneracy in the assembly process that allows for the formation of distinct crystalline structures that have a comparable equilibrium energy. We performed numerous simulations and found that HCP and FCC structures assemble with essentially the same frequency, which is expected because of the small energy difference between the two. Mixed phase structures were also frequently observed, although somewhat less so because they represent a slightly higher energy.

It should be noted that the assembled particle structure can be tuned by adjusting various factors prior to fabrication including the strength of the bias field and key particle properties. Specifically, a sufficiently strong bias field can improve the precision of particle placement by enhancing the repulsive force in various regions (e.g., the edge of a cylindrical template). However, if the bias field is too strong, it will dominate the template-induced gradient field and create chains of particles instead of ordered crystalline structures. Similarly, key particle properties can be selected to control the assembly process (e.g., particle packing) as discussed in detail in our previous work.[18] For example, as the size of the magnetic core increases, the magnetic dipole−dipole interaction, which is proportional to R_p^6 and repulsive in the final assembly, increases more rapidly than the magnetic force, which is proportional to R_p^3. Thus, particles with larger cores will tend to be less well packed and may even chain instead of forming crystalline structures.

Next, we use the Langevin model to study the self-assembly of polydisperse magnetic core−shell Fe_3O_4−SiO_2 particles. Both the magnetic core and the total particle size are generated independently using a normal distribution. A histogram of the particle and core radii are shown in panels a and b, respectively, of Figure 9. We considered a 10% variation in both of these dimensions. From this analysis we find that even with 10% polydispersity, the particles still randomly assemble into well-defined HCP, FCC, and mixed phase structures, similar to the

DOI: 10.1021/acsami.5b08310
ACS Appl. Mater. Interfaces 2015, 7, 22515−22524

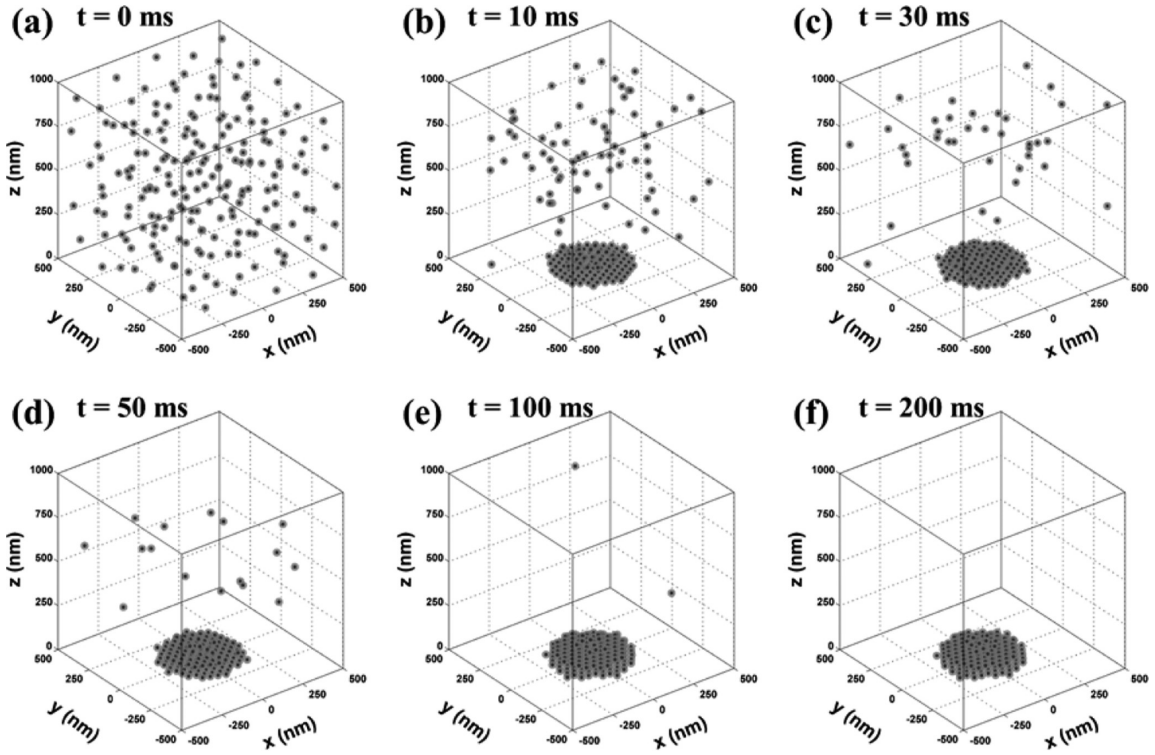

Figure 10. Self-assembly dynamics using hard-magnetic template elements; simulation images showing the particles at various times during the assembly process: (a) t = 0 ms; (b) t = 10 ms; (c) t = 30 ms; (d) t = 50 ms; (e) t = 100 ms; (f) t = 200 ms.

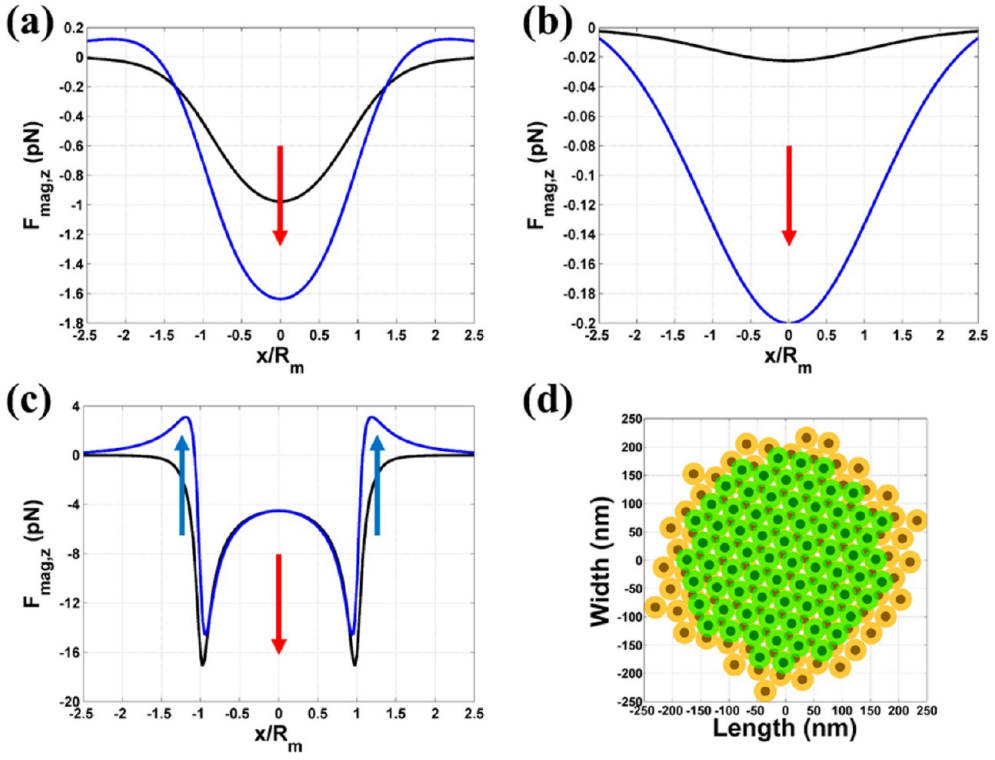

Figure 11. Force comparison and particle assembly for hard-magnetic template; comparison of the vertical force for hard-magnetic (black line) and soft-magnetic (blue line) elements: (a) z = 200 nm; (b) z = 500 nm above the element; (c) magnetic force at z = 20 nm above the element; (d) assembled particle layers.

formations obtained by the monodisperse particles. An example of an assembled four layer HCP structure is shown in Figure 9c. There is a noticeable variation in spacing gaps between adjacent particles due to irregular packing of the polydisperse particles.

It is instructive to compare the degree of particle packing for the mono- and polydisperse colloids. To this end, we computed the average in-plane interparticle spacing (as well as the standard deviation (std) in spacing) for the first three layers of

DOI: 10.1021/acsami.5b08310
ACS Appl. Mater. Interfaces 2015, 7, 22515−22524

the respective assembled structures. For the monodisperse particles we found that the spacings were slightly different for the HCP and FCC structures. For a representative HCP structure the spacings are S_1 = 0.7223 nm (std = 0.8656), S_2 = 0.8936 nm (std = 0.9419), and S_3 = 1.4982 nm (std = 1.5563), for the first, second, and third layers, respectively. The average spacing for all three layers is $S_{mono,av}$ = 0.9325 nm (std = 1.0967). Note that the particle spacing increases farther from the template element, that is, $S_3 > S_2 > S_1$. This is because the magnetic force due to the gradient field, which acts to pack the particles, decreases rapidly with distance from the template, whereas the dipole−dipole force, which acts to separate the particles, becomes more dominant. We performed the same analysis for a representative polydisperse particle structure and found that the particles were less tightly packed due to the variation in particle size. Specifically, the spacings for this structure are S_1 = 1.2488 nm (std = 1.4846), S_2 = 1.6478 nm (std = 1.8209), and S_3 = 2.6102 nm (std = 2.6616), and $S_{poly,av}$ = 1.6558 nm (std = 1.9517). Thus, the spacings for the polydisperse particle structure are 70−90% greater than the corresponding values for the monodisperse structures.

For our last study, we apply the Langevin model to investigate the difference in self-assembly using soft- and hard-magnetic elements. The former have the same magnetization as the latter as defined above, but there is no bias field. The same computational domain and particles as above are used. Simulation images showing the positions of the particles at various stages of a representative assembly are shown in Figure 10. There are two critical differences in self-assembly using hard- versus soft-magnetic templates. First, the time required to complete the former is 200 ms (Figure 10), which is an order of magnitude slower than for the soft-magnetic templates. Second, there is less spatial resolution in particle placement; that is, the particles assemble well beyond the edges of the cylinder, and only two layers are formed as compared to the tapered four-layer structures predicted using soft-magnetic templates. The slower assembly is to be expected for the hard-magnetic templates because the magnetic force is weaker, as shown in Figure 11a,b. The weaker force is due to the absence of the bias field. Specifically, the force is proportional to the induced magnetic moment in the particles, which decays rapidly with distance from the permanent magnet as compared to being saturated at all points when a bias field is present. The lack of spatial resolution is due to the fact that the magnetic force of the hard-magnetic elements is purely attractive. This is in contrast to the highly localized regions of positive and negative force that exist using soft-magnetic elements. This is illustrated in Figure 11c, which shows a comparison of a 1D plot of $F_{mag,z}$ at a height of 20 nm (middle of the first layer) for a hard- and soft-magnetic element. Note that in the former, the force is attractive (red arrow), whereas in the latter, the force is positive (blue arrow) in a narrow region just outside the edge of the soft-magnetic cylinder. This tends to confine the particles to the top of the cylinder, thereby enhancing the spatial resolution of particle placement.

Finally, while we have observed assembly of FCC, HCP, and mixed phase crystalline structures, it is possible that other structures such as body centered tetragonal structures (BCT[36,37]) may also form if the dipole−dipole interaction between the particles is sufficiently strong, that is, when it is compatible with the magnetic force due to the field gradient. In our analysis, the magnetic force due to the gradient field, which acts to pack the particles, is stronger than the dipole−dipole force. A BCT structure may occur if the gradient field is reduced over regions of the template, for example, over the center of the template as the diameter increases. We also found that the self-assembly is not necessarily a layer-by-layer process. Instead, higher layers can start forming before the lower layers are complete. We also note that templates can be used to form interesting patterned monolayer structures by adjusting the particle volume fraction as we discuss in our previous work.[17] Specifically, at a sufficiently low particle volume fraction, a monolayer assembly can be obtained by carefully choosing the particle properties, template element geometry, and bias field strength.

CONCLUSIONS

We have used two distinct complementary computational models to study the template-assisted self-assembly of multifunctional magnetic core−shell nanoparticles. We have studied both mono- and polydisperse colloids. The analysis demonstrates for the first time that the particles in both colloids randomly assemble into various distinct, energetically comparable crystalline superstructures including mixed phase structures associated with in-plane packing disorders. However, polydisperse particles assemble into less uniform crystalline structures with larger gaps between neighboring particles due to the irregular packing of the different-sized particles. In either case, the analysis implies that the template-assisted fabrication of a prescribed crystalline particle structure can be potentially problematic depending on the particle properties, even under ideal conditions. Thus, a fundamental limitation may exist in the ability to use magnetic-based self-assembly to fabricate nanostructured materials with properties that are critically dependent on the configuration and spacing of the assembled particles. Our analysis also shows that soft-magnetic templates can provide superior performance in terms of a reduced time for assembly (on the order of milliseconds) and higher spatial resolution in particle placement (on the order of nanometers) as compared to hard-magnetic templates.

In summary, the combination of field-directed self-assembly, which provides enhanced control over particle placement, and the multifunctional nature of the assembled particles opens up opportunities for transformative advances in the fabrication of novel materials[38] with unprecedented magnetic, photonic, and electronic properties. These materials could find applications in a broad range of technologies that span the fields of data storage, telecommunications, sensors, actuators, biomedicine, MEMS, etc. The findings in this work provide insight into the viability, advantages, and limitations of using self-assembly to realize these applications.

AUTHOR INFORMATION

Corresponding Author

*(E.P.F.) Mail: Department of Chemical and Biological Engineering, Department of Electrical Engineering, 113b Davis Hall, University at Buffalo (SUNY), Buffalo, NY 14260-4200, USA. E-mail: efurlani@buffalo.edu. Phone: (716) 645-1194. Fax: (716) 645-3822.

Notes

The authors declare no competing financial interest.

ACKNOWLEDGMENTS

We acknowledge financial support from the U.S. National Science Foundation, through Award CBET-1337860.

DOI: 10.1021/acsami.5b08310
ACS Appl. Mater. Interfaces 2015, 7, 22515−22524

REFERENCES

(1) Ozin, G. A.; Hou, K.; Lotsch, B. V.; Cademartiri, L.; Puzzo, D. P.; Scotognella, F.; Ghadimi, A.; Thomson, J. Nanofabrication by Self-assembly. *Mater. Today (Oxford, U. K.)* **2009**, *12* (5), 12−23.

(2) Lee, Y. S. *Self-Assembly and Nanotechnology Systems: Design,-Characterization, and Applications*; Wiley: Hoboken, NJ, USA, 2011; 480 pp.

(3) Wang, M.; He, L.; Yin, Y. Magnetic Field Guided Colloidal Assembly. *Mater. Today (Oxford, U. K.)* **2013**, *16* (4), 110−116.

(4) Yethiraj, A.; Thijssen, J. H. J.; Wouterse, A.; Van Blaaderen, A. Large-Area Electric-Field-Induced Colloidal Single Crystals for Photonic Applications. *Adv. Mater. (Weinheim, Ger.)* **2004**, *16* (7), 596−600.

(5) Lu, Y.; Yin, Y.; Xia, Y. A Self-Assembly Approach to the Fabrication of Patterned, Two-Dimensional Arrays of Microlenses of Organic Polymers. *Adv. Mater. (Weinheim, Ger.)* **2001**, *13* (1), 34−37.

(6) Shipway, A. N.; Katz, E.; Willner, I. Nanoparticle Arrays on Surfaces for Electronic, Optical, and Sensor Applications. *ChemPhysChem* **2000**, *1* (1), 18−52.

(7) Dai, Q.; Frommer, J.; Berman, D.; Virwani, K.; Davis, B.; Cheng, J. Y.; Nelson, A. High-Throughput Directed Self-Assembly of Core-Shell Ferrimagnetic Nanoparticle Arrays. *Langmuir* **2013**, *29* (24), 7472−7477.

(8) Yellen, B. B.; Friedman, G. Analysis of Repulsive Interactions in Chains of Superparamagnetic Colloidal Particles for Magnetic Template-Based Self-Assembly. *J. Appl. Phys.* **2003**, *93* (10, Part 3), 8447−8449.

(9) Yellen, B. B.; Hovorka, O.; Friedman, G. Arranging Matter by Magnetic Nanoparticle Assemblers. *Proc. Natl. Acad. Sci. U. S. A.* **2005**, *102* (25), 8860−8864.

(10) Henderson, J.; Shi, S.; Cakmaktepe, S.; Crawford, T. M. Pattern Transfer Nanomanufacturing Using Magnetic Recording for Programmed Nanoparticle Assembly. *Nanotechnology* **2012**, *23* (18), 185304/1−185304/8.

(11) Henderson, J. R.; Crawford, T. M. Repeatability of Magnetic-Field Driven Self-Assembly of Magnetic Nanoparticles. *J. Appl. Phys.* **2011**, *109* (7), 07D329/1−07D329/3.

(12) Yellen, B. B.; Fridman, G.; Friedman, G. Ferrofluid Lithography. *Nanotechnology* **2004**, *15* (10), S562−S565.

(13) Yellen, B. B.; Friedman, G. Programmable Assembly of Colloidal Particles Using Magnetic Microwell Templates. *Langmuir* **2004**, *20* (7), 2553−2559.

(14) Malik, V.; Petukhov, A. V.; He, L.; Yin, Y.; Schmidt, M. Colloidal Crystallization and Structural Changes in Suspensions of Silica/Magnetite Core-Shell Nanoparticles. *Langmuir* **2012**, *28* (41), 14777−14783.

(15) Ye, L.; Terry, B.; Mefford, O. T.; Rinaldi, C.; Crawford, T. M. All-Nanoparticle Concave Diffraction Grating Fabricated by Self-Assembly onto Magnetically-Recorded Templates. *Opt. Express* **2013**, *21* (1), 1066−1075.

(16) Mohtasebzadeh Abdul, R.; Ye, L.; Crawford Thomas, M.; Ye, L. Magnetic Nanoparticle Arrays Self-Assembled on Perpendicular Magnetic Recording Media. *Int. J. Mol. Sci.* **2015**, *16* (8), 19769−19779.

(17) Xue, X.; Furlani, E. P. Template-Assisted Nano-Patterning of Magnetic Core-Shell Particles in Gradient Fields. *Phys. Chem. Chem. Phys.* **2014**, *16* (26), 13306−13317.

(18) Xue, X.; Furlani, E. P. Analysis of the Dynamics of Magnetic Core-Shell Nanoparticles and Self-Assembly of Crystalline Superstructures in Gradient Fields. *J. Phys. Chem. C* **2015**, *119* (10), 5714−5726.

(19) Meriguet, G.; Jardat, M.; Turq, P. Structural Properties of Charge-Stabilized Ferrofluids under a Magnetic Field: A Brownian Dynamics Study. *J. Chem. Phys.* **2004**, *121* (12), 6078−6085.

(20) Meriguet, G.; Jardat, M.; Turq, P. Brownian Dynamics Investigation of Magnetization and Birefringence Relaxations in Ferrofluids. *J. Chem. Phys.* **2005**, *123* (14), 144915/1−144915/8.

(21) Lim, E. W. C. Gelation of Magnetic Nanoparticles. *Mol. Dynamics: Theor. Dev. Appl. Nanotechnol. Energy* **2012**, 215−228.

(22) Xuan, Y.; Ye, M.; Li, Q. Mesoscale Simulation of Ferrofluid Structure. *Int. J. Heat Mass Transfer* **2005**, *48* (12), 2443−2451.

(23) Davis, S. W.; McCausland, W.; McGahagan, H. C.; Tanaka, C. T.; Widom, M. Cluster-Based Monte Carlo Simulation of Ferrofluids. *Phys. Rev. E: Stat. Phys., Plasmas, Fluids, Relat. Interdiscip. Top.* **1999**, *59* (2-B), 2424−2428.

(24) Richardi, J.; Pileni, M. P.; Weis, J. J. Self-Organization of Magnetic Nanoparticles: A Monte Carlo Study. *Phys. Rev. E: Stat., Nonlinear, Soft Matter Phys.* **2008**, *77* (6−1), 061510/1−061510/9.

(25) Huang, J. P.; Wang, Z. W.; Holm, C. Computer simulations of the Structure of Colloidal Ferrofluids. *Phys. Rev. E: Stat., Nonlinear, Soft Matter Phys.* **2005**, *71* (6−1), 061203/1−061203/11.

(26) Duncan, P. D.; Camp, P. J. Aggregation Kinetics and the Nature of Phase Separation in Two-Dimensional Dipolar Fluids. *Phys. Rev. Lett.* **2006**, *97* (10), 107202/1−107202/4.

(27) Furlani, E. P. Analysis of Particle Transport in a Magnetophoretic Microsystem. *J. Appl. Phys.* **2006**, *99*, 1−35.

(28) Furlani, E. P.; Ng, K. C. Nanoscale Magnetic Biotransport with Application to Magnetofection. *Phys. Rev. E, Stat., Nonlinear, Soft Matter Phys.* **2008**, *77* (6 Part 1), 061914.

(29) Nandy, K.; Chaudhuri, S.; Ganguly, R.; Puri, I. K. Analytical Model for the Magnetophoretic Capture of Magnetic Microspheres in Microfluidic Devices. *J. Magn. Magn. Mater.* **2008**, *320* (7), 1398−1405.

(30) Furlani, E. P.; Ng, K. C. Analytical Model of Magnetic Nanoparticle Transport and Capture in the Microvasculature. *Phys. Rev. E: Stat., Nonlinear, Soft Matter Phys.* **2006**, *73* (6−1), 061919/1−061919/10.

(31) Furlani, E. P.; Sahoo, Y.; Ng, K. C.; Wortman, J. C.; Monk, T. E. A Model for Predicting Magnetic Particle Capture in a Microfluidic Bioseparator. *Biomed. Microdevices* **2007**, *9* (4), 451−463.

(32) Russel, W. B.; Saville, D. A.; Schowalter, W. R. *Colloidal Dispersions*; Cambridge University Press: Cambridge, UK, 1992.

(33) Rosensweig, R. E. Fluid Dynamics and Science of Magnetic Liquids. *Adv. Electron. Electron Phys.* **1979**, *48*, 103−199.

(34) Ding, H. L.; Zhang, Y. X.; Wang, S.; Xu, J. M.; Xu, S. C.; Li, G. H. Fe_3O_4@SiO_2 Core/Shell Nanoparticles: The Silica Coating Regulations with a Single Core for Different Core Sizes and Shell Thicknesses. *Chem. Mater.* **2012**, *24* (23), 4572−4580.

(35) Meijer, J.-M.; de Villeneuve, V. W. A.; Petukhov, A. V. In-Plane Stacking Disorder in Polydisperse Hard Sphere Crystals. *Langmuir* **2007**, *23* (7), 3554−3560.

(36) Hynninen, A.-P.; Dijkstra, M. Phase behavior of dipolar hard and soft spheres. *Phys. Rev. E: Stat., Nonlinear, Soft Matter Phys.* **2005**, *72* (5−1), 051402/1−051402/10.

(37) Pal, A.; Malik, V.; He, L.; Erne, B. H.; Yin, Y.; Kegel, W. K.; Petukhov, A. V. Tuning the Colloidal Crystal Structure of Magnetic Particles by External Field. *Angew. Chem., Int. Ed.* **2015**, *54* (6), 1803−1807.

(38) Velez, C.; Torres-Díaz, I.; Maldonado-Camargo, L.; Rinaldi, C.; Arnold, D. P. Magnetic Assembly and Crosslinking of Nanoparticles for Releasable Magnetic Microstructures. *ACS Nano* **2015**, DOI: 10.1021/acsnano.5b03783.

DOI: 10.1021/acsami.5b08310
ACS Appl. Mater. Interfaces 2015, 7, 22515−22524